The Energy Flux from the Wind to Near-Inertial Motions in the Surface Mixed Layer

ERIC A. D'ASARO

Applied Physics Laboratory, College of Ocean and Fishery Sciences, University of Washington, Seattle, WA 98105

(Manuscript received 6 November 1984, in final form 1 April 1985)

ABSTRACT

Time series of wind stress computed from long-term meteorological buoy data off North America are used to examine the forcing of surface inertial currents by the wind. A simple damped slab model of the mixed layer is used to compute $\langle \Pi(H) \rangle$, the average flux of energy from the wind to mixed layer inertial currents in a mixed layer of fixed depth H. The forcing of mixed layer inertial motions is highly intermittent. Most of the forcing occurs during the winter months, with a few dozen events accounting for typically over half the total energy flux. Major forcing events are usually associated with translating cold fronts or small lows with scales of about 100 km. The larger, synoptic scale features have little energy at the inertial frequency and thus result in only weak forcing of inertial currents. A strong seasonal signal exists in the inertial forcing. At OWS-P (50°N, 145°W), $\langle \Pi$ (50 m)$\rangle$ is largest from October to February and is a factor of 12 above the June and July values. If seasonally varying mixed layer depths are used, $\langle \Pi(H) \rangle$ is largest in October, due to the combination of a shallow mixed layer and strong forcing. The forcing of inertial motions varies with location, although comprehensive geographical coverage is not obtained here. In these data the largest wintertime average Π(50 m) is found off the east coast of North America at about 35°N. The smallest value, in the Gulf of Mexico, is four times less. Although a strong correlation between $\langle \Pi$ (50 m)$\rangle$ and $\langle u^{*3} \rangle$, the parameterized flux of energy to mixed layer turbulence, is found at OWS-P, this correlation does not hold at all other locations. This suggests that climatological models that attempt to parameterize $\langle \Pi \rangle$ in terms of $\langle u^{*3} \rangle$ will need to be tuned to local conditions.

1. Introduction

Observations of upper ocean velocities typically show energetic oscillations at nearly the local inertial frequency (Webster, 1968; Weller, 1982; D'Asaro, 1985). Within the mixed layer, numerous investigators have found that inertial currents generated by fluctuations in the local wind stress dominate the observations (Pollard and Millard, 1970; Pollard, 1980; D'Asaro, 1985; Thomson and Huggett, 1981; Weller, 1982; Price, 1981; Mayer *et al.*, 1981; Kundu, 1976; Anderson *et al.*, 1983; Krauss, 1981; McPhee, 1980; Fissel, 1983). These analyses are generally consistent with a simple damped slab model of the mixed layer originally proposed by Pollard and Millard (1970). With some significant modifications, this model can be used in regions of strong mean flow (Weller, 1982). Numerous theoretical studies (Pollard, 1969; Kroll, 1975; Pollard, 1980; Greatbatch, 1983; Price, 1981, 1983, 1985; Käse, 1978; Rubenstein, 1983; Gill, 1984) and a few observations (Käse and Olbers, 1979; Price, 1981; D'Asaro, 1985; Krauss, 1981) suggest that mixed layer inertial currents generated by the wind will propagate downward and excite inertial currents beneath the mixed layer. The rate at which energy is transferred from the mixed layer to the interior is strongly dependent on the horizontal scale of the mixed layer inertial currents and thus on the horizontal scales of the stress field. The theories indicate that, although the inertial motions produced in this way are most energetic in the mixed layer and upper thermocline, they extend throughout the ocean depth (Gill, 1984), consistent with the limited observational evidence (Fu, 1981).

Inertial motions may exchange energy with other oceanic motions, particularly with the rest of the inertial–gravity wave band. Inertial motions generated at a particular latitude may propagate equatorward, where the inertial frequency is less, and thus become part of the higher frequency, internal wave field (Fu, 1981; Munk, 1981). Conversely, higher frequency internal waves propagating poleward become, locally, near-inertial internal waves. Inertial motions may also transfer energy directly to higher frequency motions by nonlinear interactions (McComas and Müller, 1981). If, as is often hypothesized (Garrett, 1979), internal waves are responsible for much of the internal mixing in the ocean, the flux of energy into the internal wave field provides a constraint on the amount of mixing in the ocean interior (Gregg and Briscoe, 1979). Significant fluxes of energy between the internal wave field and lower frequency motions may also occur (Brown and Owens, 1981; Kunze and Sanford, 1984).

The wind is potentially one of the strongest sources of internal wave energy. It is therefore useful to estimate the magnitude and space–time distribution of energy flux from the wind into mixed layer inertial

motions. The surface wind stress field over the ocean is complex, but not random. Organized structures on many scales are apparent to even the casual observer of the weather. Oceanic inertial currents are likely to reflect this structure, filtered through the particular dynamics of these motions. This paper will investigate the statistics of wind forced inertial motions and their relationship to atmospheric structures.

The annual and interannual variability of upper ocean temperature and salinity in midlatitudes is clearly related to atmospheric forcing. One-dimensional models employing the turbulent kinetic energy equation are commonly used in modeling this variability (Niiler and Kraus, 1977). Three mechanisms of turbulent kinetic energy production are usually invoked: i) turbulence production by near-surface, wind driven shear, usually parameterized by a multiple of ρu^{*3}, where ρu^{*2} is the wind stress and ρ is the density of the upper ocean; ii) turbulence production by near-inertial frequency shear at the base of the mixed layer which is bounded above by the energy flux into near-inertial motions (Pollard *et al.,* 1973); and iii) turbulence production by convection due to the surface fluxes of heat and salt. The first two mechanisms transfer energy from the wind stress to oceanic turbulence, but in very different ways: i) depends only on the wind stress magnitude, while ii) depends on the near-inertial frequency component of wind stress, as explored in this paper. The wind stress magnitude, and thus i), is relatively easy to compute over large areas of the ocean. The near-inertial component of wind stress, and thus ii), cannot reliably be computed from routine meteorological data (Thomson, 1983). Seasonal and climatological models of the upper ocean must necessarily ignore ii) or attempt to parameterize it in terms of more accessible meteorological quantities.

In this paper, the following questions are addressed:

1) What is the statistical distribution of inertial motion forcing by the wind?

2) Which structures in the atmosphere are associated with the generation of inertial motions in the ocean?

3) What is the seasonal, geographical and interannual variation of the forcing of inertial motions by the wind?

4) Do the characteristics of the atmosphere allow any simplifications in the modeling of oceanic inertial motions?

5) Can the average energy flux to inertial motions be parameterized in terms of ρu^{*3}?

Ideally, these questions should be addressed by comparing measured mixed layer inertial currents and wind stresses. Except in a few locations, such simultaneous wind and oceanographic data are not available. The studies cited above suggest, however, that a simple slab model gives a first order estimate of the generation of mixed layer inertial currents by the wind. Estimates of the forcing of mixed layer inertial currents are made here using this model and existing wind data. This paper is therefore a study of one aspect of the wind field over the ocean, namely its ability to excite mixed layer inertial currents.

The data and model are introduced in Section 2. The above questions are addressed in Section 3; the results are summarized in Section 4 and discussed in Section 5.

2. Analysis techniques

a. Data sources

Measurements of wind speed and direction were obtained from meteorological buoys, maintained by NDBC (NOAA Data Buoy Center; Hamilton, 1980), and from Ocean Weather Station P (OWS-P), maintained by the Canadian Weather Service, via the National Climatic Center archives. The locations of the buoys are shown in Fig. 1. Measurements from the NDBC buoys were made at 10 m height; the OWS-P measurements were made at 21 m and were adjusted to 10 m height assuming a logarithmic profile. Wind stress was computed from the 10 m wind velocity using Garratt's (1977) drag coefficient, ignoring stratification effects, and edited by inspection for obviously bad points.

Uncertainty in the wind stress estimates is a major source of error in the following calculations (see Appendix). The model requires a time series of wind stress with a time resolution sufficient to resolve the inertial frequency. Much of the data used here has a resolution of 3 h. This is barely sufficient, and may produce a 20% underestimation of the energy flux to inertial motions. The use of the Garratt (1977) drag coefficient, rather than the Large and Pond (1981) drag coefficient, and the neglect of stratification effects may result in a 20% overestimation of the energy flux to inertial motions. In addition, stresses estimated using a drag coefficient contain significant errors during times of rapidly changing wind (Large and Pond, 1981). D'Asaro (1985) estimates an error of 20% in the magnitude of the computed inertial currents for one storm due to this effect.

b. Inertial current model

The time series of wind stress are used to drive a damped slab model of mixed layer currents (Pollard and Millard, 1970). For mixed layer depth H, density ρ, inertial frequency f, and wind stress components τ_x and τ_y, the equations for the mixed layer velocity components u and v are

$$\frac{du}{dt} - fv = \frac{\tau_x}{H\rho} - ru \tag{1a}$$

$$\frac{dv}{dt} + fu = \frac{\tau_y}{H\rho} - rv, \tag{1b}$$

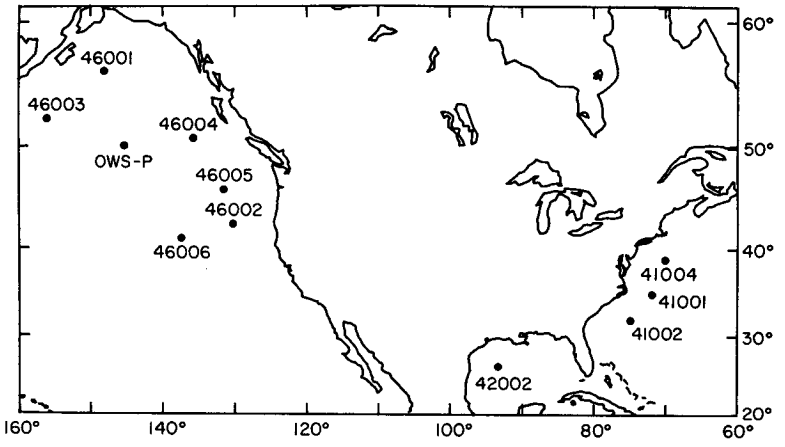

FIG. 1. Locations of surface meteorological observations used in this study. All are NDBC buoys and are labeled with their WMO code except for Ocean Weather Station P (OWS-P).

where r is an artificial damping constant that parameterizes the transfer of energy from the mixed layer to the deeper ocean. Many comparisons of the model simulations with measured mixed layer currents can be found in the references cited in the Introduction. The best simulations are usually obtained with $1/r$ in the range of 2 to 10 days, and H set to the measured mixed layer depth. Realistic simulations clearly require $r^2 \ll f^2$.

The equations are more easily expressed in terms of the complex quantities

$$Z = u + iv \tag{2}$$

$$T = \frac{(\tau_x + i\tau_y)}{\rho} \tag{3}$$

$$\omega = r + if \tag{4}$$

so that the model equations are

$$\frac{dZ}{dt} + \omega Z = \frac{T}{H}. \tag{5}$$

The behavior of these equations is well known. When the wind stress is zero,

$$Z = Z_0 e^{-ift-rt}. \tag{6}$$

The velocity vector rotates clockwise with time frequency f and exponentially decays at the rate r. These are damped inertial oscillations. For a steady wind the model has a steady solution,

$$Z_E = \frac{T}{\omega H}. \tag{7}$$

This is the Ekman transport, modified slightly by the frictional damping, spread uniformly over the mixed layer depth H. For an arbitrary wind stress, the solution is divided into time varying inertial and Ekman components. Equation (7) defines the Ekman component. The rest of the solution corresponds to the inertial oscillations

$$Z_I = Z - Z_E, \tag{8}$$

which are described by

$$\frac{dZ_I}{dt} + \omega Z_I = -\frac{dZ_E}{dt} = -\frac{d(T/H)}{dt}\frac{1}{\omega}$$

$$= -\frac{dT}{dt}\frac{1}{\omega H} - \frac{d(1/H)}{dt}\frac{T}{\omega}. \tag{9}$$

Inertial oscillations, as defined here, are excited only by variations in T/H. The mixed layer depth typically changes much more slowly than the wind stress (Large *et al.*, 1984) so that dH/dt can usually be ignored and the inertial oscillations are driven primarily by variations in T.

The frequency response of this model for constant H is obtained by Fourier transforming (1) in time, yielding the response of the mixed layer currents $Z(\sigma)$ to forcing $T(\sigma)$ at frequency σ.

$$Z = \frac{-r + i(f + \sigma)}{(\sigma^2 - f^2 - r^2 - 2ir\sigma)}\frac{T}{H}. \tag{10}$$

In the oceanic parameter range, $r^2 \ll f^2$, an "inertial resonance" occurs at $\sigma \approx f$, so the mixed layer currents respond primarily to the near-inertial frequency, clockwise rotating, component of wind stress.

This paper discusses the characteristics of the wind field as filtered through Eq. (9). In particular, the energy transferred from the wind to inertial currents will be estimated. An energy equation for the inertial motions is obtained by multiplying (9) by Z_I^*, the complex conjugate of Z_I,

$$\frac{d|\tfrac{1}{2}Z_I|^2}{dt} = -r|Z_I|^2 - \mathrm{Re}\left[\frac{Z_I}{\omega^* H}\frac{dT^*}{dt}\right]$$

$$= -r|Z_I|^2 - \Pi(H). \tag{11}$$

The change in inertial energy per unit mass is the sum of a frictional decay proportional to r and the flux of energy from the wind into inertial motions. This flux will be denoted by $\Pi(H)$ so that its dependence on the (constant) mixed layer depth is explicit. The integral of $\Pi(H)$ over a given time period, for example a storm or a season, will be denoted by $P(H)$.

The model contains two parameters, the mixed layer depth H and the decay constant r. For $r^2 \ll f^2$ the average inertial current amplitude is inversely proportional to both H and r, as can be found by integrating (10) over frequency assuming that $T(\sigma)$ is smooth near $\sigma = f$ (Fissel *et al.*, 1976), and $\Pi(H)$ is inversely proportional to H and roughly independent of r.

c. *Assumptions and approach*

Several assumptions are necessary in the following analysis. First, H is assumed to vary slowly over an inertial period. Although long time series of wind stress are available at many locations over the ocean, the corresponding measurements of mixed layer depth are rarely available. Accordingly, dH/dt in (9) usually cannot be computed. The wind stress vector commonly changes by 100% (Fig. 2) during a storm, while 10 m of mixed layer deepening in an inertial period is considered large (Tabata, 1961; Large *et al.*, 1984). Thus, except for very shallow mixed layers, the relative variations in T on an inertial time scale are much larger than those of H, and the variations in H can be neglected in computing $d(T/H)/dt$. Clearly, this approximation does not apply for mixed layers with a strong diurnal variation. Second, wind stress variations are assumed to be independent of the ocean, specifically H and Z, and approximately statistically stationary on time scales of a season and space scales of several hundred kilometers. Thus, for example, a given storm is not considered unique, but is assumed representative of many similar storms occurring at different times and/or locations. Under these assumptions a constant value of H can be used in the model simulations, and the energy flux for any particular H computed afterward. A standard value of $H = 50$ m will be used in all such calculations, and the corresponding energy flux denoted by Π (50 m). The energy flux for mixed layer depth H is given by $\Pi(H) = \Pi\ (50\ \text{m})\ (50\ \text{m}/H)$.

The average value of $\Pi(H)$ is insensitive to the value of r. Several different values of r are therefore used here, depending on the goals of the analysis. Here, $1/r = 4$ days is used to obtain the most realistic inertial currents and time series of $\Pi(H)$; $r = 0$ is used to display the initial response of the model to an isolated storm since, in this case, all changes in Z_I are due to the wind stress; and $r = f/2\pi$ is used to isolate the response of the model to individual storms when several storms occur in succession. Typically, storms occur with a frequency greater than $1/r$, so inertial currents following a storm will depend not only on the wind stress during that storm, but on several earlier storms also. The response to each storm can be isolated by using an artificially large value of r, as long as $r^2 \ll f^2$. Varying r does not seriously bias the mean of $\Pi(H)$, but does affect its variability. The number of independent estimates of $\Pi(H)$ in a given record is inversely proportional to r. Thus, averages of $\Pi(H)$ computed with large values of r will be more stable than those computed with small values.

Values of τ are available at 1 or 3 hour intervals, depending on the data. At 50°N $1/f$ is only 2.5 hours, comparable to the sampling interval of the data, so the solution to the equations depends to some degree on the method of integration. Equation (9) was integrated numerically by assuming a linear variation of τ between the data points and solving the equations analytically in this domain for Z and Π. This method of integration was selected over higher order quadrature methods or spectral methods because of its efficiency and because the computed inertial currents at any given time are due only to stresses at previous times. Details of these calculations and estimates of the errors due to the limited time resolution of the data are included in the Appendix.

3. Results

a. *A typical simulation*

Wind data from NDBC buoy 46004 are used to drive the model, assuming $H = 50$ m and $1/r = 4$ days, for a 3 month period in the winter of 1978–79. The results are shown in Fig. 2. The wind stress is plotted as a vector in Fig. 2a, with north vertical and the base of the vector giving the time of the observation on the bottom axis. The amplitude and phase of the resulting inertial current are plotted as a series of vectors in Fig. 2b. A pure inertial current would, for example, be plotted as a vector of constant amplitude and phase, with the phase equal to the phase that the inertial current would have on 0000 GMT 1 January 1900 (Julian date). A clockwise rotating current with constant frequency greater than the inertial frequency would be plotted as a vector that rotates clockwise with time. The flux of energy to inertial currents, Π (50 m), and its time integral, $P\ (50\ \text{m}) = \int_0^t \Pi\ (50\ \text{m})\ dt$, are plotted in Fig. 2c and 2d respectively. Similar plots, but with more time resolution, are shown in Figs. 4–7.

The wind stress in Fig. 2a is highly variable, reflecting the large number of storms that pass over the buoy during this period. The simulated inertial currents vary more slowly than the wind stress because the model integrates over a time $1/r$ and because the wind events that lead to strong forcing of the inertial currents are highly intermittent. This intermittency

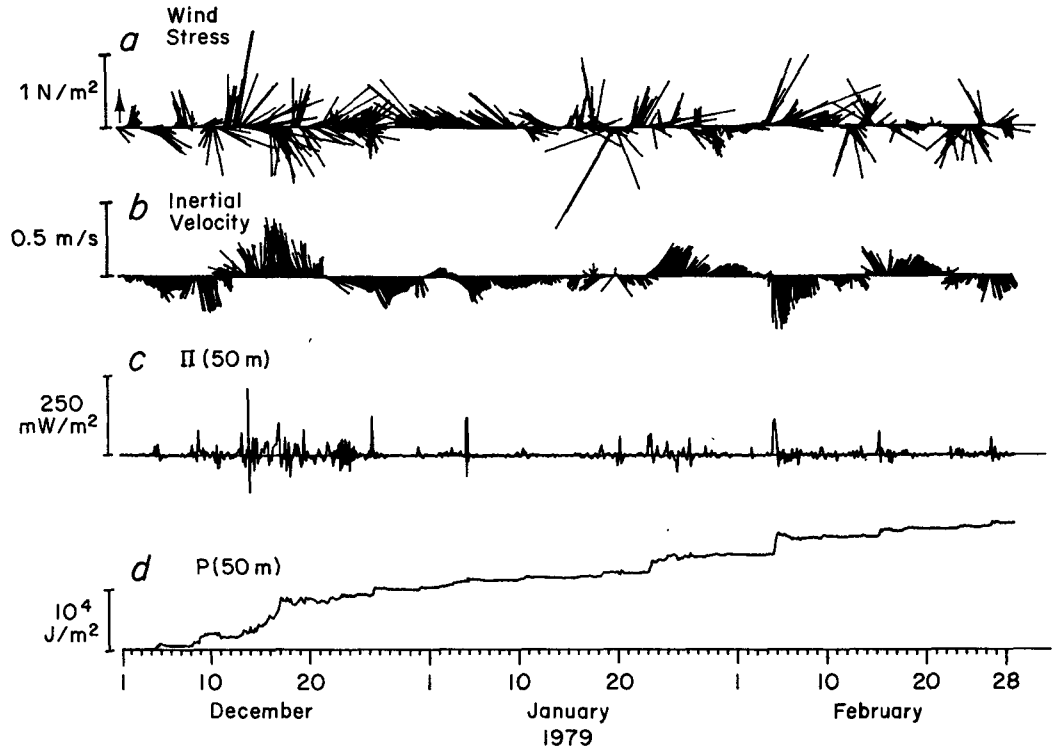

FIG. 2. Time series for buoy 46004: (a) wind stress, (b) model inertial velocity computed with $1/r = 4$ days and $H = 50$ m, (c) Π (50 m), the energy flux from the wind to the inertial currents, and (d) P (50 m) = $\int_0^t \Pi$ (50 m) dt.

is seen more clearly in the time series of Π (50 m) (Fig. 2c), which is dominated by a small number of spikes, and in P (50 m) (Fig. 2d), which has a step-like appearance. The excitation of inertial currents occurs primarily in a small number of short events, such as those on 22 January and 4 February.

Π (50 m) can be both positive and negative; i.e., the wind can both accelerate and decelerate the inertial currents (Pollard, 1980; D'Asaro, 1985). Thus, although the wind on average does work on the ocean, as indicated by the general increase in P (50 m) (Fig. 4d), a given inertial event, such as that on 11 December, may extract energy from the ocean. This occurs when $\tau \cdot \mathbf{U}$ is negative, so that the wind stress τ opposes the surface current $\mathbf{u}$. The near surface shears in both the atmospheric and oceanic boundary layers are increased in this case, and thus the energy is lost to enhanced turbulent dissipation in both the ocean and atmosphere.

b. *Probability distribution of inertial forcing*

The probability distribution of Π (50 m) computed from 10 years of winds at OWS-P (1963–1972) using $1/r = 4$ days is plotted in an energy preserving form in Fig. 3a. The light line plots the probability distribution of Π (50 m) as a function of $\log_{10}$[Π (50 m)] and is scaled such that the area between any two values of Π (50 m) is proportional to the probability of Π (50 m) being between those values. The heavy line similarly plots the contribution of each value of Π (50 m) to P (50 m), the total energy transferred. Because Π (50 m) can have both positive and negative values, two curves are required; positive values of Π are plotted with solid lines, and negative values with dashed lines. Formally, $p[\Pi]d\Pi$ is the probability of Π having a value with $d\Pi$ of Π. In Fig. 3, $\Pi p[\Pi]$ is plotted with a light line as a function of $\log_{10}(\Pi)$. $\Pi^2 p[\Pi]$ is the contribution of each value of Π to P and is plotted with a heavy line.

The distribution of Π (50 m) is highly non-Gaussian and intermittent (kurtosis = 360). The values of Π range from a minimum of −376 mW m^{-2} to a maximum of 1110 mW m^{-2}. The cumulative contribution to P (50 m), $\int_{-\infty}^{\Pi} \Pi p(\Pi) d\Pi / P$, reaches 0.5 at the 99.3 percentile, so the top 0.7% of the samples, or 60 hours per year, contributes half of the total energy flux.

The mean value of Π (50 m), 2.4 mW m^{-2}, is nonzero because positive values of Π (50 m) are more likely than negative values. Typically, large positive values of Π are followed by large negative values (see Figs. 4–7), which partially cancel their effect on the ocean. Much of the mean value of Π is

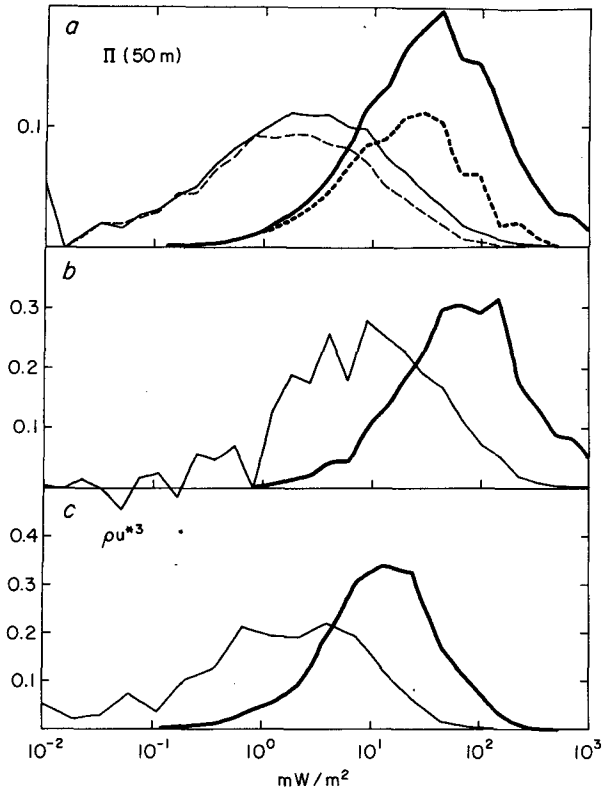

FIG. 3. Probability distributions of various quantities computed from OWS-P data, 1963–72, using Eqs. (9) and (11) with $1/r = 4$ days. Light curves are probability density. Heavy curves are contribution to the mean value. All are plotted in "energy preserving" coordinates so that the area under the curve is proportional to the probability density (light) and to its contribution to the mean value (heavy). (a) Probability distribution of Π (50 m), the flux of energy from the wind to mixed layer inertial currents. Solid line is for positive values; dashed for negative values. (b) The antisymmetric part of a), i.e., $p(\Pi) - p(-\Pi)$. (c) Probability distribution of ρu^{*3}, where u^* is the friction velocity.

thus contributed by the largest positive values of Π that are not canceled by the following negative values. This is shown in Fig. 3b, which plots the antisymmetric part of Π, $p(\Pi) - p(-\Pi)$. The top 90% of the flux is contributed by the top 50% of the samples, i.e., values of Π greater than about 9 mW m^{-2}; the top 20% of the flux is contributed by the top 1.5% of the samples, i.e., values of Π greater than about 150 mW m^{-2}. Values of Π one to two orders of magnitude larger than the mean contribute most of the flux. These events must necessarily be quite infrequent, and the flux of energy from the wind to inertial motions is thus clearly intermittent. In fact, Π is sufficiently intermittent that 10 years of data are only marginally sufficient to resolve the positive tail of $\Pi^2 p(\Pi)$, and thus the mean flux.

For comparison, the probability distribution of u^{*3} is plotted in Fig. 3c. As found by Elsberry and Camp (1978), u^{*3} is also very intermittent (kurtosis = 82), but less so than Π (50 m). The 10 year time series appears sufficient to resolve the distribution of u^{*3}.

c. *Storm types*

The generation of inertial motions, because of its intermittency, is dominated by a number of distinct "events." The relationship of these "inertial events" to atmospheric features was investigated by examining wintertime data from several NDBC buoys in detail. "Inertial events" were identified in each record by large values of Π (50 m) ($r = f/2\pi$). Synoptic weather charts prepared by the National Weather Service (NWS) were examined for each event to identify the associated meteorological feature. The features observed generally fall into the following classifications.

1) COLD FRONT

A moving cold or occluded cold front is commonly associated with the generation of inertial oscillations. Figure 4 shows the passage of such a cold front over NDBC buoy 41001 off the east coast of North America. The panels are the same as in Fig. 2, but are plotted with greater time resolution. Here and in the following few figures, a value of $r = 0$ has been used to best display the inertial vectors. The light vertical line at 1500 GMT 7 January denotes the time of the NWS chart (Fig. 4e), which is also approximately the time that the front passed over the buoy. Π (50 m) shows a sharp spike at this time. This front is an efficient generator of inertial motions because the wind stress is large and rotates rapidly in the clockwise direction as the front passes.

2) LOW

A moving low is commonly associated with the generation of inertial oscillations. Figure 5e shows a small low traveling eastward between two NDBC buoys off the west coast of North America. At the southerly buoy a clockwise rotating wind stress results in the efficient generation of inertial currents. At the northerly buoy, the wind stress is similar in magnitude but rotates anticlockwise with time and therefore produces less energetic inertial currents. This asymmetry in the response to a translating, symmetric storm has been noted previously for hurricanes (Price, 1980). Here, however, the storm itself is asymmetrical, with a cold front on its southern side and a much smoother structure on its northern side. Much of the generation of inertial motions at the southern buoy appears to be due to the rapid change in the wind stress vector associated with the front rather than the slower rotation of the wind stress due to the motion of the low. The north–south asymmetry is therefore due to both the asymmetry in the response of the inertial currents to a symmetric, translating storm, and the asymmetry of the storm itself.

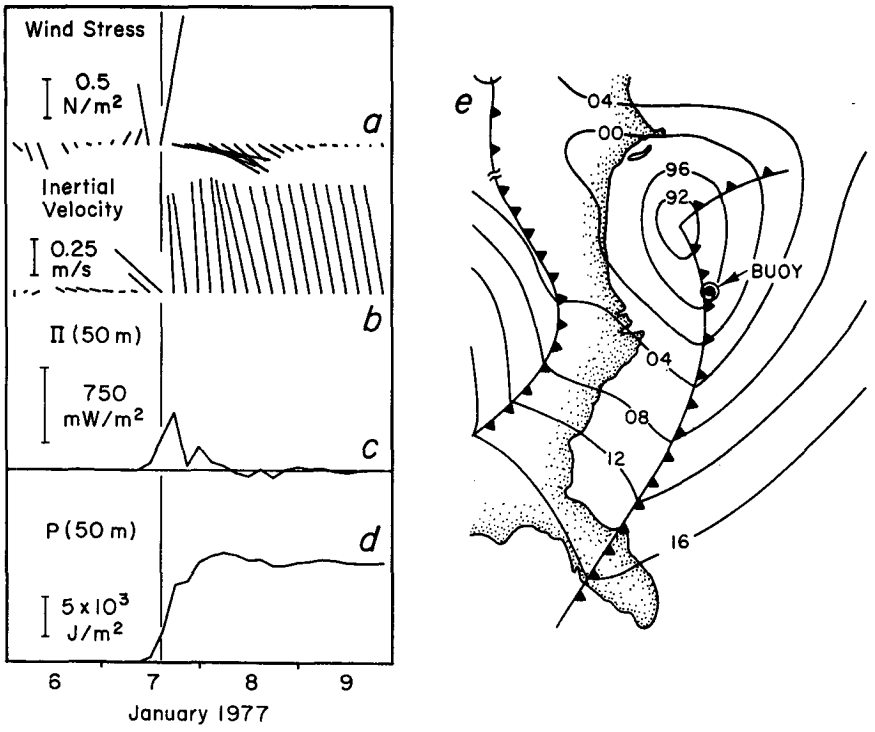

FIG. 4. Inertial motions resulting from a cold front at buoy 41001; (a)–(d) as in Fig. 2. Vertical line denotes time of NWS map.

3) HURRICANES

Although hurricanes are clearly a form of translating low, they are dramatically more energetic than typical midlatitude lows. This is well illustrated in Fig. 6. They are excellent generators of inertial motions because of their large wind stress which changes on an inertial time scale. Price (1981, 1983, 1985) discusses the generation of inertial motions by hurricanes.

4) MORE COMPLEX PATTERNS

At times, two or more of the above elements occur in rapid succession, resulting in a hybrid case. A pattern common off the southeastern United States involves a wave on the preexisting polar front, which grows into a large low. Early in this process, the low is only a small perturbation traveling along the front. The time history of the wind stress at a given point is thus the result of this combined front-low feature. Later in the development of the system, the low grows sufficiently to be distinct from the front and a situation such as that in Fig. 4 develops.

Typically, the generation of inertial oscillations can be considered to be the sum of distinct events, clearly separated in time. At times, however, the forcing more closely resembles a continuous excitation. This can be seen in mid-December in Fig. 4, and also in Fig. 7. The NWS charts show a cold front followed by a series of waves, some of which are associated with fronts, spanning the eastern North Pacific (Fig. 7e). The initial front generates inertial currents which are then almost continuously modified for several days by the following features. Π (50 m) rarely remains small for more than a fraction of an inertial period. The generation of inertial currents during this period cannot be associated with a single feature on the weather chart.

5) GENERAL OBSERVATIONS

The absence of certain common features in the above list is notable. Large stationary lows, or steady zonal jets, although they may contain strong wind stresses, do not excite inertial oscillations. With a very few exceptions, neither do highs, ridges, or warm fronts. The dominant time synoptic scales of the atmosphere are longer than $1/f$ (Fissel *et al.*, 1976), so the dominant synoptic features do not excite inertial motions. However, atmospheric features smaller than the synoptic scale (500–2000 km) will be advected at a typical speed of 10 m s^{-1}. Features with a scale of about 100 km, *in the advection direction,* will advect past a given location with a time scale of $1/f$ in midlatitudes. It is therefore these smaller scale features, fronts, small waves, and secondary small lows that excite inertial oscillations. Thus, there is a potentially strong connection between meteorology on this scale and the study of oceanic inertial motions.

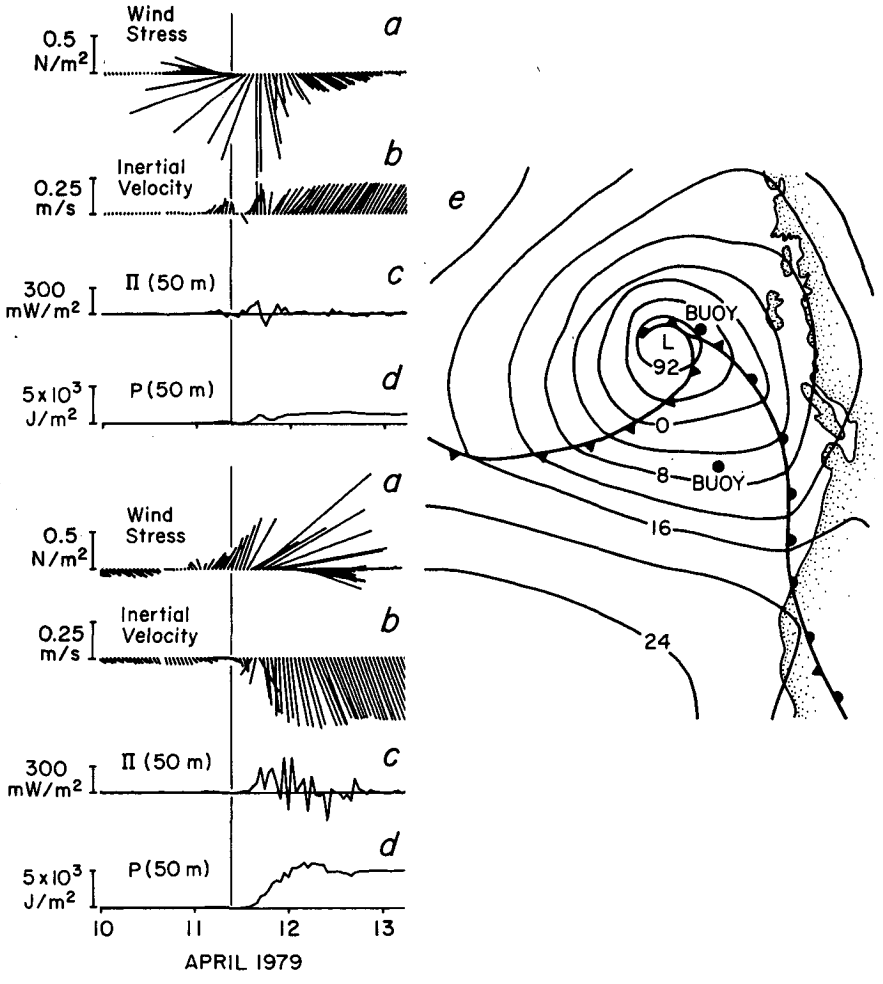

FIG. 5. Inertial motions resulting from a low that passed between buoys 46004 (upper panels) and 46005 (lower panels); (a)–(d) as in Fig. 4.

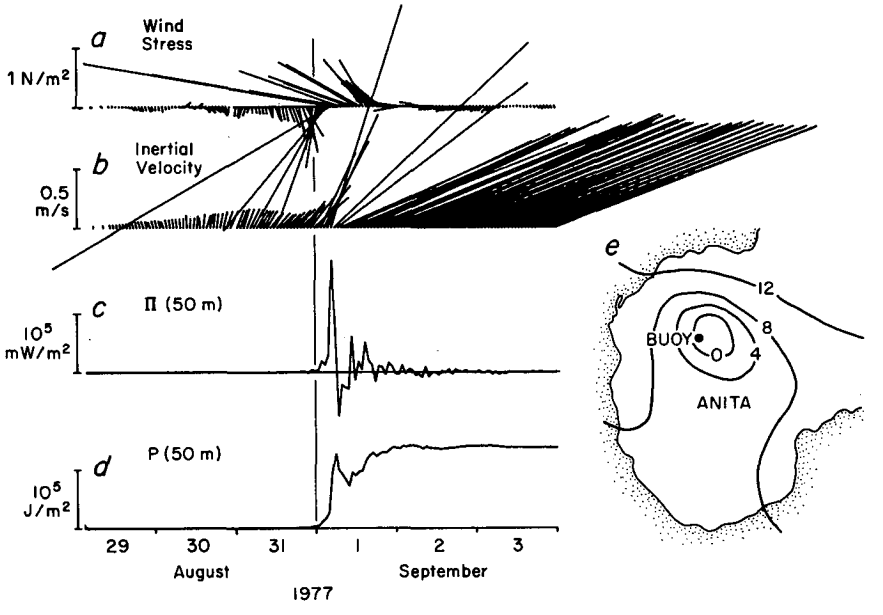

FIG. 6. Inertial motions resulting from a hurricane passing near buoy 42002; (a)–(d) as in Fig. 4. Notice change in scale for (c) and (d).

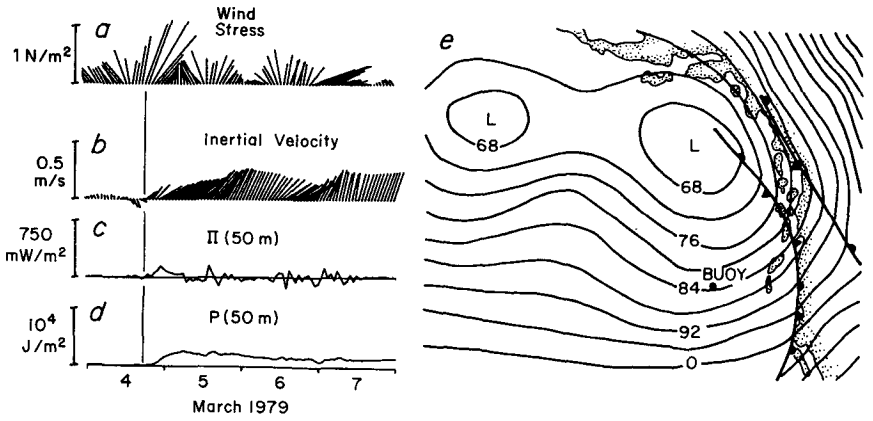

FIG. 7. Inertial motions resulting from a complex synoptic situation at buoy 46004; (a)–(d) as in Fig. 4.

d. *Distribution of storm types*

1) THE RANDOM STORM TIMING HYPOTHESIS

The strong intermittency of inertial motion generation allows a mathematical simplification of the generation process. If the wind stress is modeled as a series of delta functions, each representing an "inertial event," the response of a linear model, such as the one used here, is the linear superposition of the response of the model to each event. If a few events dominate the solution, this is a highly efficient representation. The forcing function for the inertial currents is

$$F = -\frac{dT}{dt}\frac{1}{\omega H} = \sum_i F_i \delta(t - t_i), \tag{12}$$

where F_i is the magnitude of the forcing event at time t_i. The solution to (9) with this forcing is

$$Z_I(t) = \sum_i F_i H(t - t_i) e^{-(if+r)(t-t_i)}, \tag{13}$$

where $H(t) = 1$ if $t > 0$ and 0 otherwise. From (11) the work done by the wind on the inertial motions is

$$\int_0^\infty \Pi dt = \mathrm{Re}\left[\int_0^\infty Z_I(t) F^*(t) dt\right] \tag{14}$$

$$= \mathrm{Re}\left[\sum_{i \geq j} F_i F_j^* e^{(if-r)(t_i-t_j)}\right]. \tag{15}$$

If the phase of the individual forcing events is random relative to an inertial period, $e^{(if-r)(t_i-t_j)}$ is a random variable with mean zero unless $i = j$, and the total work is

$$P = \sum_i |F_i|^2 = \sum_i P_i. \tag{16}$$

In this "random storm timing" approximation, the contribution of each storm to the total work done by the wind is, on the average, independent of the other storms, even if the inertial currents from one storm have not died out at the time of later storms. This approximation can be applied to any linear model of storm response.

2) ANALYSIS

A detailed analysis of the distribution of storm types associated with the generation of inertial oscillations was made for two winters' data from three buoys using the random storm timing hypothesis. P_i is estimated for each storm from Π (50 m) with $r = f/2\pi$. With this value of r, the inertial currents generated by a given storm usually decay before the next storm arrives so that a definite value of P_i can be computed for each storm. A storm is defined to occur whenever Π, filtered with an inertial period-wide $\cos^2$ filter, is greater than 0.05 mW m^{-2}. Also P_i is computed from the integral of Π (50 m) from two inertial periods before to two inertial periods after the time of maximum filtered Π. Only storms with P_i greater than 500 J m^{-2} are considered. For each event, the NWS maps were examined. The event was then classified as a front (F), low (L), or mixed front and low (FL), or, if none of these, other (O). A small number of events did not correspond to any feature on the NWS charts, or contained buoy data errors; these were classified as unknown (U). If several events occurred so close together that the response of the ocean to each event alone could not be determined, the entire sequence was labeled complex (C).

Histograms of the work done during each event are shown in Figs. 8, 9, and 10. The bin size increases logarithmically with increasing work, in order to compensate for the decreasing density of storms. The area in each bin is proportional to the total work done by its events. Within a given range of P (50 m), the contribution of each type of storm is shown, along with the number of storms of that type in parentheses. The contribution of complex storms (C)

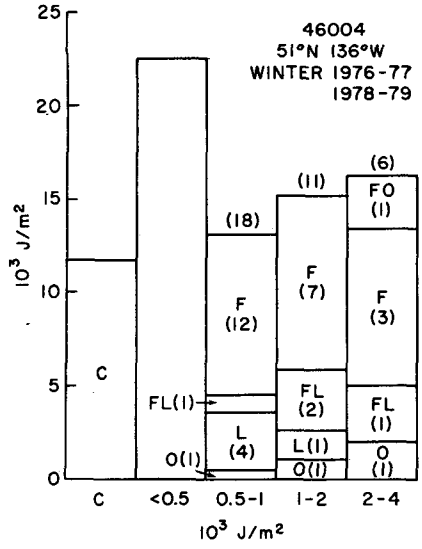

FIG. 8. Histogram of P_i, the energy transferred to inertial currents in storm i, at buoy 46004 during the winters of 1976/77 and 1978/79. Storms are classified as fronts (F), lows (L), combined front and low (FL), other (O) and unknown (U) on the basis of NWS maps. Number of storms in each category is indicated in parentheses. Energy transferred during a series of closely spaced storms is classified as complex (C). Energy transferred during periods of weak storms is not classified but is included in the "<0.5" bin.

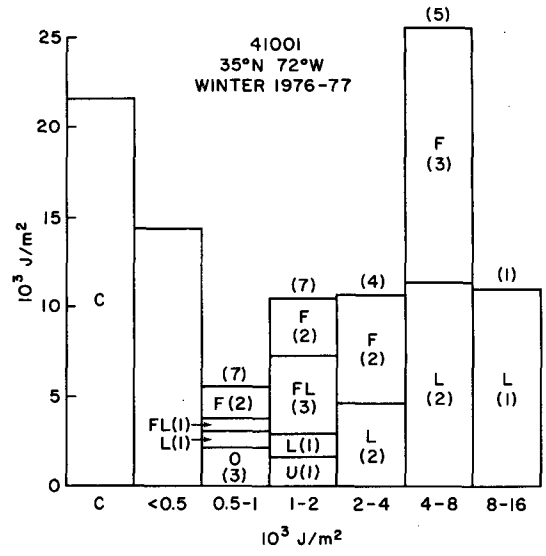

FIG. 10. As in Fig. 9 at buoy 41001 during the winter of 1976/77.

is plotted separately. The difference between the work done by all the classified storms and the total work for the entire record is used to compute the work due to weak storms. The results are tabulated in Table 1. The contribution of each class of storm for each buoy is given as a fraction of the total energy flux, and as a fraction of all the flux due to the classified storms only.

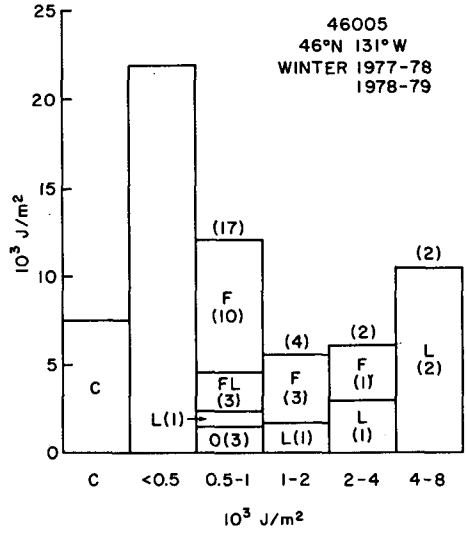

FIG. 9. As in Fig. 8 at buoy 46005 during the winters of 1977/78 and 1978/79.

A relatively small number of events account for a large fraction of the total work. Between 15 and 33 events per 6-month winter, excluding the complex cases, account for between half and two-thirds of P (50 m). At 41001, one event accounts for 12% of P (50 m). Fronts and lows are the dominant types of storms, with fronts being somewhat more common and lows being somewhat more energetic.

e. *Seasonal variability*

The seasonal cycle of inertial energy flux was estimated at OWS-P for 10 years of data, 1963 through 1972 (Fig. 11), using $r = f/2\pi$. Individual monthly averages of Π (50 m) are plotted as dots in Fig. 11b, and the 10 year monthly averages are plotted as a line. The maximum flux occurs from October to February and is about 12 times the minimum flux in June and July. The seasonal cycle of Π (50 m) roughly parallels the seasonal cycle of ρu^{*3} (Fig. 11a) with a somewhat greater amplitude and less sinusoidal shape.

Here $\Pi(\langle H \rangle)$, where $\langle H \rangle$ is the monthly mean mixed layer depth, is a better estimate of the true energy flux from the wind to inertial motions. The average mixed layer depth (Giovondo and Robinson, 1965; Fig. 11d) varies from 25 m in midsummer to over 100 m in late winter. $\Pi(\langle H \rangle)$ ignores any year-to-year correlation between the inertial energy flux and the mixed layer depth. The rms variation of mixed layer depth, shown in Fig. 11d, is relatively small so the effect of this correlation should also be small. $\Pi(\langle H \rangle)$ is largest in October, when the wind forcing is strong and the mixed layer depth is shallow. Although the wind forcing is still strong later in the winter, the mixed layer depth is greater, resulting in less energy flux. The maximum flux is a factor of

TABLE 1. Energy flux to inertial currents classified by storm type.

Buoy		Storm type F	L	FL	O	U	All classified storms	C	"<0.5"
41001	Percent total flux	26	30	5	2	2	65	22	14
10/76–3/77	Percent classified flux	40	46	8	3	3	100	—	—
	Number of storms	9	7	4	3	1	33	9	—
46004	Percent total flux	32	6	9	9	0	56	15	28
10/76–3/77	Percent classified flux	57	11	16	16	0	100	—	—
10/78–3/79	Number of storms	21	5	4	5	0	43	8	—
46005	Percent total flux	22	25	3	3	0	65	11	35
10/77–3/78	Percent classified flux	33	38	5	5	0	100	—	—
10/78–3/79	Number of storms	13	5	3	4	0	29	4	—

about 7 above the minimum flux. The annual average energy flux is 1.44 mW m^{-2}.

Another measure of the seasonal variability is the average number of storms per month. Here, a storm occurs whenever Π (50 m), filtered with a two inertial period-wide $\cos^2$ filter, is greater than 5 mW m^{-2}.

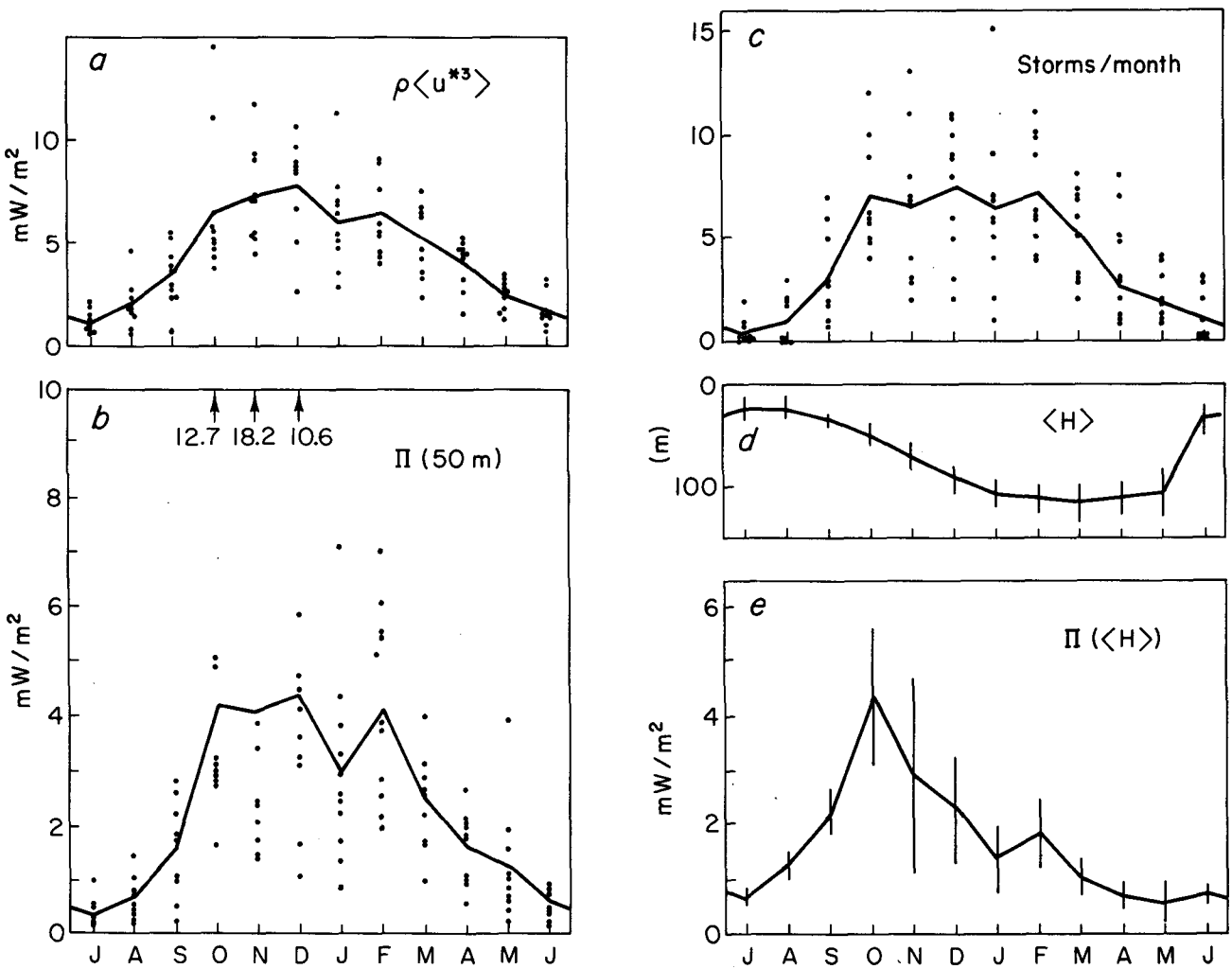

FIG. 11. Seasonal cycle of inertial energy flux, mixed layer depth and ρu^{*3} at OWS-P, 1963–72. (a) Monthly average ρu^{*3} for each month (dots) and 10 year average (line). (b) Monthly average Π (50 m) for each month (dots) and 10 year average (line) ($r = f/2\pi$). Three points are off scale, indicated at top. (c) Number of storms per month for each month (dots) and 10 year average (line). (d) Monthly average mixed layer depth and standard deviation from Giovondo and Robinson (1965). (e) Monthly average $\Pi(\langle H \rangle)$ and standard deviation. Computed from (b) and (d).

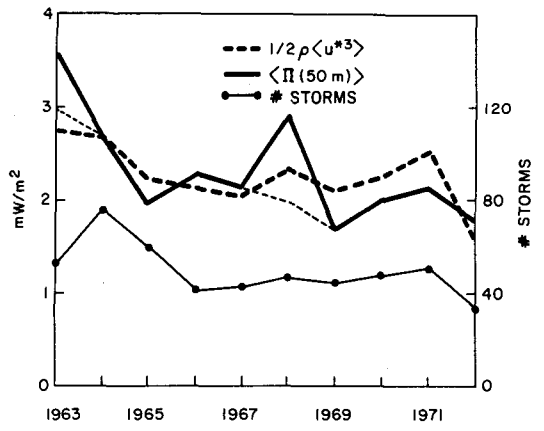

FIG. 12. Yearly average values of $\Pi(H)$, computed as in Fig. 11b (heavy line), ρu^{*3} (dashed line), and number of storms (light line, right axis) for OWS-P, calendar years 1963–72. Dotted heavy lines show the effect of removing the three off-scale storms in Fig. 11b from $\langle \Pi\ (50\ \text{m}) \rangle$.

Storms with multiple peaks contribute multiply to this count. The number of storms is plotted for each month in Fig. 11c along with the 10 year average. The maximum number of storms occur from October to February, roughly 6.5 per month; the minimum number occurs in July, less than 0.5 on the average. This is very similar to the annual cycle of Π (50 m) in Fig. 11b.

f. Interannual variability

The annual average of Π (50 m), the number of storms per year, and the average value of ρu^{*3} are plotted in Fig. 12 for each calendar year from 1963 to 1972. The three variables are correlated to some degree, with $\langle \Pi\ (50\ \text{m}) \rangle$ displaying the most variability, followed by $\langle \rho u^{*3} \rangle$ and the number of storms. They all show a slight decrease over the decade, although this is barely resolvable above the year-to-year variability.

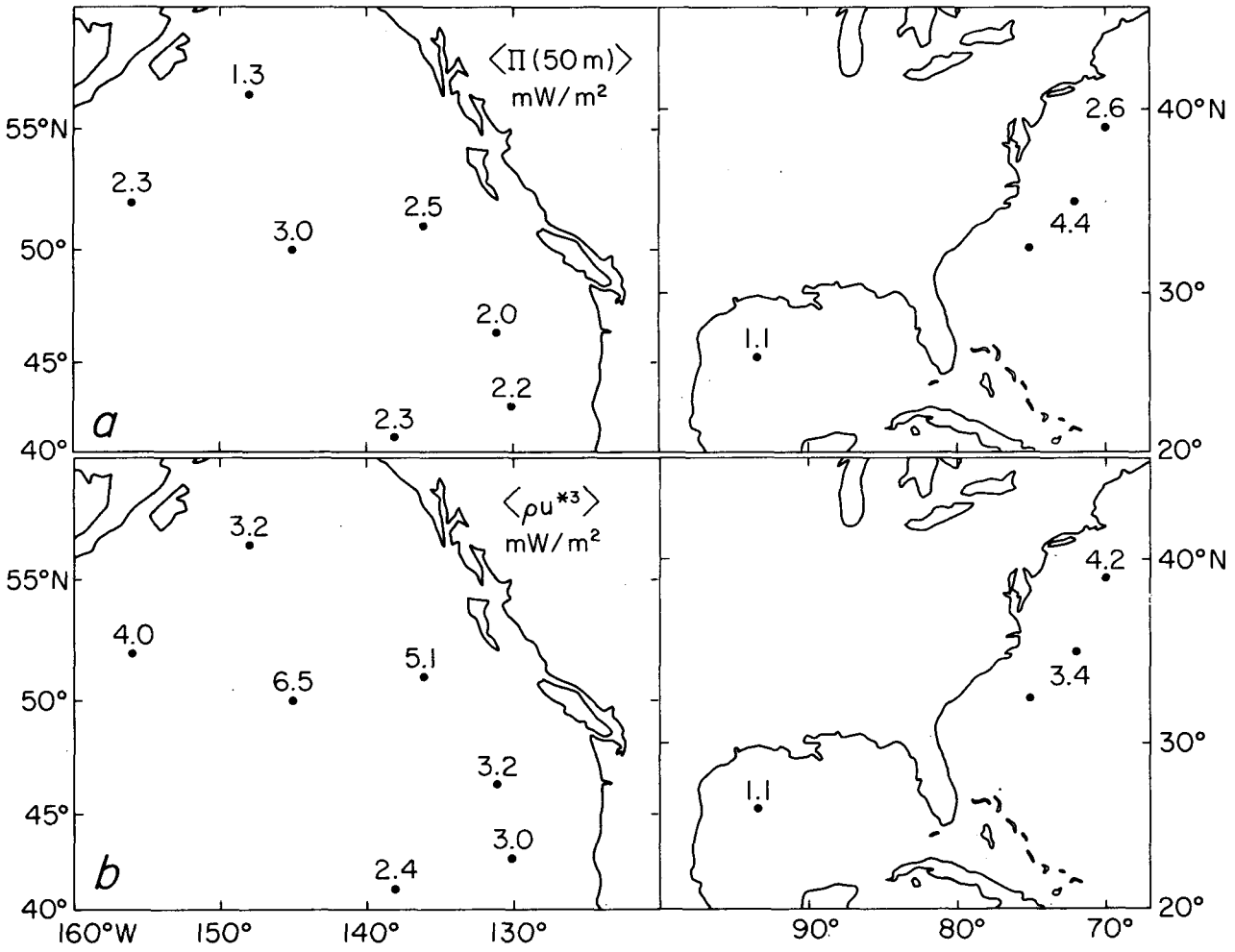

FIG. 13. Geographical variability of (a) $\langle \Pi\ (50\ \text{m}) \rangle$, computed as in Fig. 11b, (b) $\rho \langle u^{*3} \rangle$, (c) the number of storms per month, and (d) the mean wind stress magnitude, for the winter months (October–March) only. Different time periods are used at each buoy as indicated in Table 2.

In both Figs. 11 and 12, a few very large events have a noticeable impact on the averages of Π (50 m). In the 10 year period, the average flux in any given month is generally within a factor of 2 of the 10 year average (Fig. 11). However, for 3 months, October 1963, November 1968, and December 1963, the monthly average energy flux is greater than twice the mean (and off the top of the plot in Fig. 11b). In all three cases, this is the result of a single, large storm. The November 1968 storm increases the 10 year mean energy for that month by 60% over what it would have been if that year had been excluded. The light dashed lines in Fig. 12 illustrate the substantial effect of removing these storms from the annual means for 1963 and 1968. On the other hand, the large energy flux for 1964 appears to be due to a larger number of storms in that year. Thus, although there is clearly a seasonal and possibly an interannual variation in the flux of energy to inertial motions, this is superposed on a large stochastic variability.

g. Geographical variability

Values of the wintertime (October–March) average Π (50 m) ($r = f/2\pi$), the number of storms, mean wind stress magnitude, and $\langle \rho u^{*3} \rangle$ are plotted in Fig. 13 for a number of buoys. The years used for each buoy are listed in Table 2. Typically, 10–20 months of data are used in each average, with some months in each winter omitted because of bad or missing data. These estimates therefore have as many data points as the monthly estimates in Fig. 11, and should have similar confidence limits.

Distinct geographical variation in the forcing is evident. In the Pacific, all of the quantities show a broad maximum at about 50°N, consistent with the patterns of storminess previously found by Blackmon *et al.* (1977) and Haney *et al.* (1981). Off the Atlantic and Gulf coasts, the pattern is less simple. The mean wind stress decreases with latitude while ⟨Π (50 m)⟩, and the number of storms is maximum at buoys 41001 (34°N) and 41002 (32°N). At these buoys ⟨Π

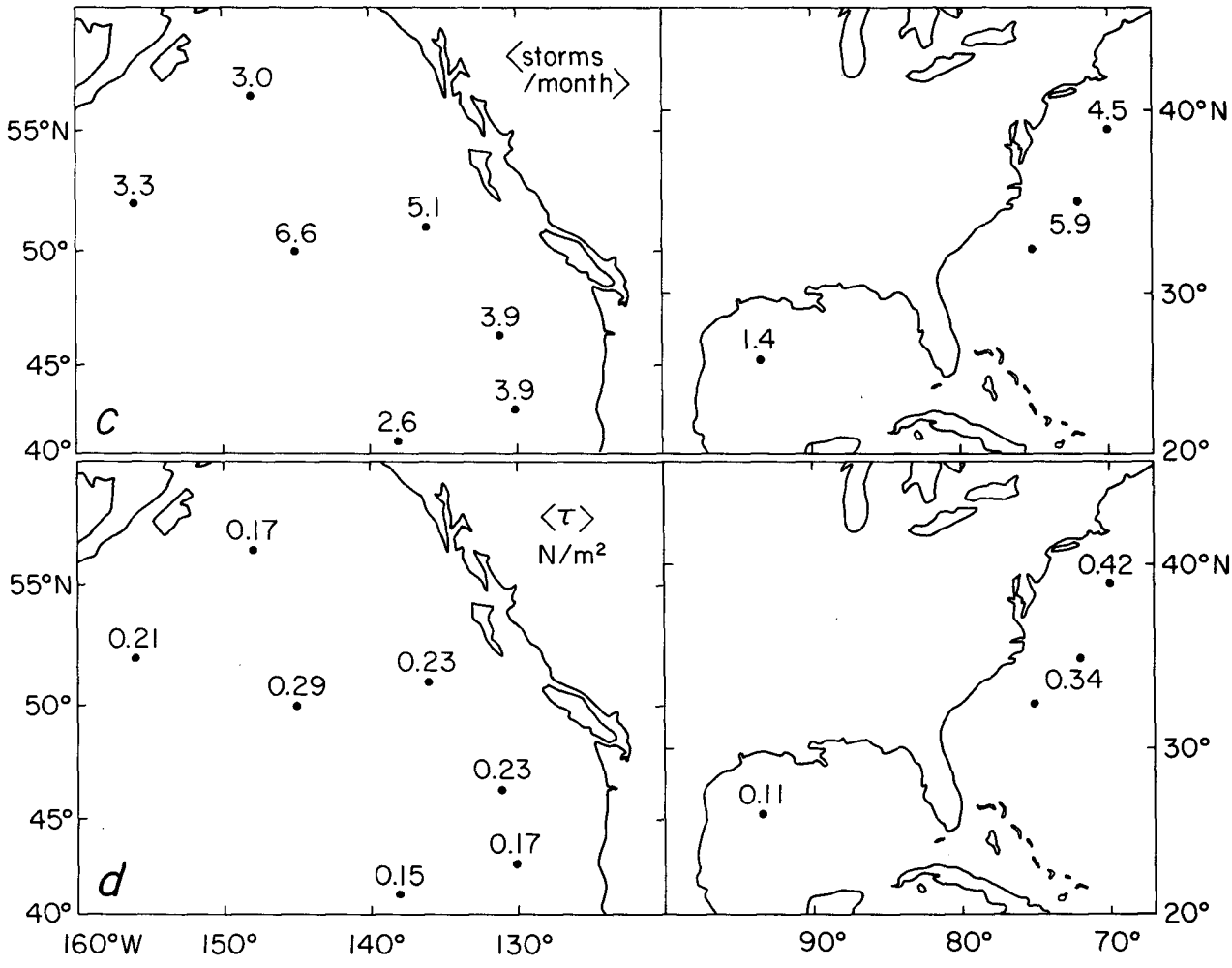

FIG. 13. (*Continued*)

TABLE 2. Buoy data used in Fig. 13.

WEST buoy	Winters	Number of months	EAST buoy	Winters	Number of months
46001	74–75	4	44004	77–78	6
	75–76	4		78–79	6
	76–77	4		Total:	12
	77–78	5	41001	76–77	6
	Total:	17	41002	74–75	6
46003	76–77	6		75–76	3
	77–78	6		76–77	2
	78–79	4		77–78	6
	Total:	16		Total:	23
46004	76–77	6	42002	76–77	6
	78–79	6		77–78	4
	Total:	12		78–79	6
OWS-P	64–72	60		Total:	16
46005	77–78	6			
	78–79	6			
	Total:	12			
46006	77–78	6			
	78–79	6			
	Total:	12			
46002	75–76	2			
	76–77	6			
	77–78	6			
	78–79	6			
	Total:	20			

(50 m)$\rangle$ is larger than at OWS-P, although both the mean wind stress and $\langle u^{*3}\rangle$ are smaller. Examination of the time series suggests that this is due to sharper fronts off the Atlantic coast than off the Pacific coast, presumably because of the combined effects of continental cold air advection, and warm water advection by the Gulf Stream. This is also a region of strong cyclogenesis (Sanders and Gyakum, 1980). The smallest values of all variables occur in the Gulf of Mexico. Although they are not discussed in detail here, hurricanes occur only at the Atlantic and Gulf buoys and make a substantial contribution to the total inertial energy flux in the summer and fall.

h. Inertial energy flux and ρu^{*3}

In Fig. 14 $\langle\Pi$ (50 m)$\rangle$ is plotted against $\rho\langle u^{*3}\rangle$. At OWS-P (Fig. 14a) a strong correlation is observed both for the 10 year monthly averages (dots) and for the annual averages (+); $\langle\Pi$ (50 m)$\rangle/\rho\langle u^{*3}\rangle$ is approximately 0.5 and increases with $\rho\langle u^{*3}\rangle$. Thus, if the wind generates turbulent kinetic energy at approximately $0.4\rho\langle u^{*3}\rangle$ (Davis *et al.*, 1981a,b), the wind fluxes roughly equal amounts of energy, on the average, to inertial and turbulent motions in the upper ocean, for a mixed layer depth of 50 m. Since $\Pi(H)$ is proportional to $1/H$, the inertial energy flux is proportionally larger for shallower mixed layers.

When the data from various buoys are compared (Fig. 14b) $\langle\Pi$ (50 m)$\rangle$ and $\langle u^{*3}\rangle$ are not so well correlated. The other buoys generally have a somewhat larger value of $\langle\Pi$ (50 m)$\rangle$ for the same $\langle u^{*3}\rangle$. This may be partially due to differences between the instrumentation at OWS-P and the other buoys. The data from off Cape Hatteras (41001 and 41004), however, have two to three times the value of $\langle\Pi$ (50 m)$\rangle$ for the same $\langle u^{*3}\rangle$ as the OWS-P data. Similarly, the more southerly buoys on both coasts (46002, 46006, 46005, and 42002) tend also to lie farthest above the OWS-P data. These geographical variations are undoubtedly due to geographical variations in the weather patterns. Since $\langle\Pi$ (50 m)$\rangle$ depends on variations in the wind stress while $\rho\langle u^{*3}\rangle$ depends only on its magnitude, their ratio depends on the unsteadiness of the wind stress. The large value of $\langle\Pi$ (50 m)$\rangle/\rho\langle u^{*3}\rangle$ off Cape Hatteras may be due to the large number of small, rapidly growing storms in this region (Sanders and Gyakum, 1980) as compared to the prevalence of large, mature storms near OWS-P.

It does not appear, therefore, that a general relationship between $\langle\Pi$ (50 m)$\rangle$ and $\rho\langle u^{*3}\rangle$ can be found that is valid for all the locations considered here. Models that parameterize inertial motions in terms of $\langle u^{*3}\rangle$ will probably have to be tuned to local conditions.

4. Summary

Simulations of mixed layer inertial currents using winds measured at a number of midlatitude buoys reveal the following features:

1) The forcing of mixed layer inertial motions is highly intermittent, with a few dozen events accounting for typically over half the annual energy flux.

2) Major forcing events are usually associated with translating cold fronts or small lows. Although they may have large wind stresses, the larger synoptic scale features do not excite inertial motions.

3) A strong seasonal signal exists in the inertial forcing. At OWS-P (50°N, 145°W) the strongest forcing is from October to February and is a factor of 12 above the June and July values. The energy transferred to the ocean is inversely proportional to the mixed layer depth. If the variation of the mixed layer depth is taken into account, the maximum energy flux is in October, due to the combination of a relatively shallow mixed layer and strong forcing.

4) The forcing of inertial motions varies with location, although comprehensive geographical coverage is not obtained here. The largest wintertime average energy flux from the wind to near-inertial motions, uncorrected for the depth of the mixed layer, is found off Cape Hatteras. The smallest value, in the Gulf of Mexico, is four times less.

5) The flux of energy from the wind to mixed

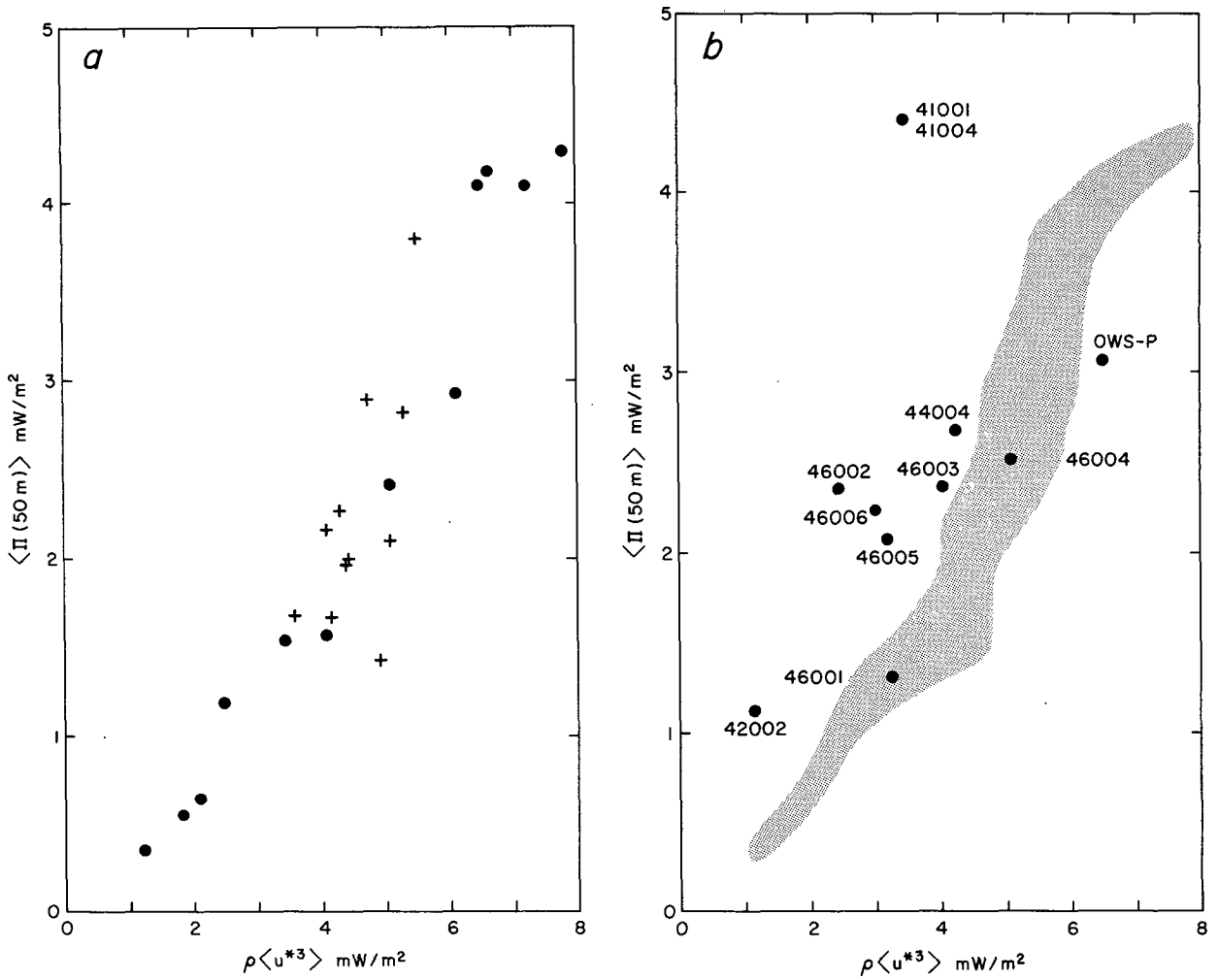

FIG. 14. Scatter plots of $\rho\langle u^{*3}\rangle$ against $\langle \Pi\ (50\ \mathrm{m})\rangle$ for (a) annual cycle at OWS-P (dots) and interannual variability at OWS-P (+), and (b) buoy data from Fig. 13; OWS-P data from (a) are stippled.

layer inertial motions is comparable to the flux of energy to mixed layer turbulence, and increases with decreasing mixed layer thickness. Although a strong correlation between the inertial forcing $\rho\langle u^{*3}\rangle$ is found at OWS-P, this same relationship does not hold at all locations. This suggests that models that attempt to parameterize mixed layer inertial motions in terms of $\rho\langle u^{*3}\rangle$ will have to be tuned to local conditions.

5. Discussion

The forcing of inertial motions is intermittent for two reasons. First, as discussed above, the forcing is primarily by strong atmospheric features with a scale near 100 km. These features are highly intermittent in the atmosphere. Second, the inertial currents generated by a wind event are proportional to τ_I [Eq. (1)]. The rate of energy transfer, Π, is therefore proportional to $\tau \cdot \mathbf{u}$ and thus $|\tau|^2$. Since τ is proportional to U^2 or U^3, where U is the wind speed, then $\Pi \approx |U|^4$ or $|U|^6$. Thus, even if U were nearly Gaussian, Π would be highly non-Gaussian; small intermittencies in the distribution of U are greatly enhanced in the distribution of Π.

These data clearly demonstrate that the forcing of inertial motions is highly intermittent in time. The spatial distribution of the forcing is less well described. Although the strong forcing events observed at a given buoy are almost always associated with a distinct meteorological feature, such as a cold front, it is not clear whether the forcing is equally strong at all points along this feature, or at all times in its life. Cold fronts, for example, are not uniform along their length, but exhibit waves, kinks, and cloud clusters on a variety of scales (Houze and Hobbs, 1982). Does the strength of the inertial frequency forcing vary along the front, do local "hot spots" exist, or is the forcing uniform over many hundreds of kilometers? These questions are important in determining the

horizontal structure of the mixed layer and sea surface temperature response to storms, and to understanding the propagation of inertial motions out of the mixed layer. They can be answered only from the analysis of two-dimensional wind stress fields. Such wind fields are far more difficult to obtain than the single point measurements discussed here and are the subject of work in progress.

Realistic models of the response of the midlatitude ocean to atmospheric forcing will require realistic wind forcing as input. Current synoptic products are not sufficient to predict mixed layer inertial currents (Thomson, 1983). Satellite scatterometers (Brown, 1983) appear able to provide sufficient spatial resolution (better than 100 km), but are unlikely to provide the 3 hour temporal resolution required at midlatitudes. A useful wind field might be obtained, however, by horizontally advecting the wind stress field obtained on a given satellite pass with the synoptic scale flow to obtain a space-time wind field. For climatological models, an artificial ensemble of random translating storms with a statistical distribution similar to that in Fig. 2 may be sufficient. Such models will probably require a parameterization of the amplitude of the inertial forcing such as that attempted in Fig. 14.

Inertial motions are observed to be highly intermittent both in the mixed layer and below. The present work suggests that this may partially be due to the intermittency in their rate of generation by the wind stress. Other mechanisms, such as the interaction of inertial motions with the geostrophic flow (Kunze and Sanford, 1984) or merely interference between groups of waves (Gill, 1984), may also be important.

Finally, these results show a clear seasonal and geographical signal in the flux of energy into mixed layer, near-inertial motions. Assuming that at least some of this energy propagates into the interior as near-inertial, internal waves, there should be a corresponding seasonal and geographical variation in the near-inertial energy level below the mixed layer. Fu (1981) and Munk (1981) hypothesize that much of the structure of oceanic near-inertial waves is due to their latitudinal propagation. In these models, higher frequency internal waves propagate poleward until their frequency approaches the local value of f. Here they are reflected equatorward. Their amplitude is locally increased at the turning point, creating an inertial peak. This mechanism requires near-inertial waves to propagate latitudinally over distances on which f varies significantly, say 1000 km. Accordingly, near-inertial motions generated by the wind should also propagate these distances and result in a seasonal signal in higher frequency internal waves at latitudes south of the major storm tracks. The seasonal cycle, if any, and statistics of inertial motions below the mixed layer as a function of latitude and depth should provide useful information on the latitudinal propagation of inertial motions.

Acknowledgments. I thank T. Sanford, who started this project, and W. Large, who provided a coded version of his drag law program. E. Kunze, D. Lai and N. Larson made useful comments on the original manuscript. This work was supported by the Office of Naval Research, Contracts N00014-81-K-0095 and N00014-84-C-0111.

APPENDIX

1. Computation of inertial response

Given the wind stress at times t_1 and t_2 and inertial current Z_{I1} at t_1, Eq. (9) can be solved for Z_{I2} using

$$Z_{I2} = Z_{I1}e^{-\omega\Delta t} - \frac{T_t}{H\omega^2}(1 - e^{-\omega\Delta t}), \qquad \text{(A1)}$$

where $T_t = \Delta T/\Delta t$ is the change in T over the interval Δt. Here T is assumed to vary linearly with time. The average flux of energy transferred to the inertial motions during this interval is evaluated by integrating (11) using (A1),

$$\Pi = \mathrm{Re}\left\{\frac{T_t^*}{\Delta t|\omega|^2 H}\left[\left(Z_{I1} + \frac{T_t}{\omega^2 H}\right)(e^{-\omega\Delta t} - 1) + \frac{T_t}{\omega H}\Delta t\right]\right\}. \qquad \text{(A2)}$$

This is evaluated and plotted at time $t = t_2$.

2. Sampling error

The wind stress data used here are mostly sampled at $\Delta t = 3$ hours, with occasional sampling at 1 h. The error due to the finite Δt was estimated by simulating the response of the model to a wind stress rotating either clockwise or counterclockwise at the inertial frequency corresponding to 50°N. Using $\Pi(H)$ as $\Delta t \to 0$ as a reference, $\Pi(H)$ is 2% low for $\Delta t = 1$ h, and 20% low for $\Delta t = 3$ h for both the clockwise and anticlockwise cases. The sampling error is therefore significant, but not large enough to affect the qualitative conclusions.

3. Stress estimate errors

The drag formula of Garratt (1977) is used in these calculations without any correction for stratification of the boundary layer. The errors due to omitting the stratification correction and to systematic errors in this drag law were estimated by redoing the calculation for NDBC buoy 41001 using the Large and Pond (1981) drag law with stratification correction. The air-sea temperature difference, and thus the stratification correction, is large and highly variable at this site. The energy flux computed using the Large and Pond formulae is approximately 80% of the value found using the uncorrected Garratt formula. This is true not only for the average flux (81%), but also for the energy flux in individual storms (79% ± 5% rms). This difference represents not only the effect of strat-

ification, but also the differences between the two neutral drag laws. These appear to have only a quantitative effect; again, the major qualitative conclusions are unaffected.

REFERENCES

Anderson, I., A. Huyer and R. Smith, 1983: Near-inertial motions off the Oregon coast. *J. Geophys. Res.*, **88**(C10), 5960–5973.

Blackmon, M. L., J. M. Wallace, N. Lau and S. L. Mullen, 1977: An observational study of the Northern Hemisphere wintertime circulation. *J. Atmos. Sci.*, **34**, 1040–1053.

Brown, R. A., 1983: On a satellite scatterometer as an anemometer. *J. Geophys. Res.*, **88**(C3), 1663–1673.

Brown, E. D., and W. B. Owens, 1981: Observations of the horizontal interactions between the internal wave field and the mesoscale flow. *J. Phys. Oceanogr.*, **11**, 1474–1481.

D'Asaro, E., 1985: Upper ocean temperature structure, inertial currents, and Richardson numbers observed during strong meteorological forcing. *J. Phys. Oceanogr.*, **15**, 943–962.

Davis, R. E., R. DeSzoeke, D. Halpern and P. P. Niiler, 1981a: Variability in the upper ocean during MILE. Part I: The heat and momentum balances. *Deep-Sea Res.*, **28A**(12), 1427–1451.

——, —— and P. Niiler, 1981b: Variability in the upper ocean during MILE. Part II: Modelling the mixed layer response. *Deep-Sea Res.*, **28A**(12), 1453–1475.

Elsberry, R. L., and N. T. Camp, 1978: Ocean thermal response to strong atmospheric forcing: I. Characteristics of the forcing events. *J. Phys. Oceanogr.*, **8**, 206–214.

Fissel, D. B., 1983: Tidal currents and inertial oscillations in northwestern Baffin Bay. *Arctic*, **35**(1), 201–210.

——, S. Pond and M. Miyake, 1976: Spectra of surface atmospheric quantities at Ocean Weathership P. *Atmosphere*, **14**(2), 77–97.

Fu, L. L., 1981: Observations and models of inertial waves in the deep ocean. *Rev. Geophys. Space Phys.*, **19**, 141–197.

Garratt, J. R., 1977: Review of drag coefficients over oceans and continents. *Mon. Wea. Rev.*, **105**, 915–929.

Garrett, C., 1979: Mixing in the ocean interior. *Dyn. Atmos. Oceans*, **3**, 239–265.

Gill, A., 1984: On the behavior of internal waves in the wakes of storms. *J. Phys. Oceanogr.*, **14**, 1129–1151.

Giovando, L. F., and M. K. Robinson, 1965: Characteristics of the surface layer in the northeast Pacific Ocean. *Fish. Res. Bd. Can.*, Manuscript Report Series.

Greatbatch, R. J., 1983: On the response of the ocean to a moving storm: The nonlinear dynamics. *J. Phys. Oceanogr.*, **13**, 357–367.

Gregg, M. C., and M. G. Briscoe, 1979: Internal waves, finestructure, microstructure, and mixing in the ocean. *Rev. Geophys. Space Phys.*, **17**, 1524–1548.

Hamilton, G. D., 1980: NOAA data buoy office programs. *Bull. Amer. Meteor. Soc.*, **61**, 1012–1017.

Haney, R. L., M. S. Risch and G. C. Heise, 1981: Wind forcing due to synoptic storm activity over the North Pacific Ocean. *Ocean. Atmos.*, **19**, 128–147.

Houze, R. A., and P. V. Hobbs, 1982: Organization and structure of precipitating cloud systems. *Advances in Geophysics*, Vol. 24, Academic Press, 225–315.

Käse, R. H., 1978: Calculations of the energy transfer by the wind to near-inertial internal waves. *Deep-Sea Res.*, **26**, 227–232.

——, and D. J. Olbers, 1979: Wind-driven inertial waves observed during Phase III of GATE. *Deep-Sea Res.*, **26**, 191–216.

Krauss, W., 1981: The erosion of the thermocline. *J. Phys. Oceanogr.*, **11**, 425–433.

Kroll, J., 1975: The propagation of wind-generated inertial oscillations from the surface into the deep ocean. *J. Mar. Res.*, **33**, 15–49.

Kundu, P. K., 1976: An analysis of inertial oscillations observed near Oregon Coast. *J. Phys. Oceanogr.*, **6**, 879–893.

Kunze, E., and T. B. Sanford, 1984: Observations of near inertial waves in a front. *J. Phys. Oceanogr.*, **14**, 566–581.

Large, W. G., and S. Pond, 1981: Open ocean momentum flux measurements in moderate to strong winds. *J. Phys. Oceanogr.*, **11**, 324–336.

——, J. C. McWilliams and P. P. Niiler, 1984: Drift buoy observations of the upper ocean's thermal response during STREX, (unpublished manuscript).

Mayer, D. A., H. O. Mofjeld and K. D. Leaman, 1981: Near-inertial internal waves observed on the outer shelf in the Middle Atlantic Bight in the wake of Hurricane Belle. *J. Phys. Oceanogr.*, **11**, 87–106.

McComas, C. H., and P. Müller, 1981: The dynamic balance of internal waves. *J. Phys. Oceanogr.*, **11**, 970–986.

McPhee, M. G., 1980: A study of oceanic boundary-layer characteristics including inertial oscillations at three drifting stations in the Arctic Ocean. *J. Phys. Oceanogr.*, **10**, 870–884.

Munk, W., 1981: Internal waves and small scale processes. *Evolution of Physical Oceanography: Scientific Surveys in Honor of Henry Stommel*, B. A. Warren and C. Wunsch, Eds., The MIT Press, 264–291.

Niiler, P. P., and E. B. Kraus, 1977: One-dimensional models of the upper ocean. *Modelling and Prediction of the Upper Layers of the Ocean*, E. B. Kraus, Ed., Pergamon Press, 143–172.

Pollard, R. T., 1969: On the generation by winds of inertial waves in the ocean. *Deep-Sea Res.*, **17**, 795–812.

——, 1980: Properties of near-surface inertial oscillations. *J. Phys. Oceanogr.*, **10**, 385–398.

——, and R. C. Millard, 1970: Comparison between observed and simulated wind generated inertial oscillations. *Deep-Sea Res.*, **17**, 813–821.

——, R. B. Rhines and R. O. R. Y. Thompson, 1973: The deepening of the wind mixed layer. *Geophys. Fluid Dyn.*, **3**, 381–404.

Price, J. F., 1981: Upper ocean response to a hurricane. *J. Phys. Oceanogr.*, **11**, 153–175.

——, 1983: Internal wave wake of a moving storm. Part I: Scales, energy budget and observations. *J. Phys. Oceanogr.*, **13**, 949–965.

——, 1985: Internal wave wake of a moving storm. Part II: Parameter dependence. Submitted to *J. Phys. Oceanogr.*

——, C. N. K. Mooers and J. C. Van Leer, 1978: Observation and simulation of storm-driven mixed-layer deepening. *J. Phys. Oceanogr.*, **8**, 582–599.

Rubenstein, D. M., 1983: Vertical dispersion of inertial waves in the upper ocean. *J. Geophys. Res.*, **88**(C7), 4368–4380.

Sanders, F., and J. R. Gyakum, 1980: Synoptic-dynamic climatology of the "bomb." *Mon. Wea. Rev.*, **108**, 1589–1606.

Tabata, S., 1961: Temporal changes of salinity, temperature, and dissolved oxygen content of the water at Station "P" in the Northeast Pacific Ocean and some of their determining factors. *J. Fish. Res. Bd. Can.*, **18**(6), 1073–1124.

Thomson, R. E., 1983: A comparison between computed and measured oceanic winds near the British Columbia Coast. *J. Geophys. Res.*, **88**(C4), 2675–2683.

——, and W. S. Huggett, 1981: Wind-driven inertial oscillations of large spatial coherence. *Atmos.-Ocean*, **19**, 281–306.

Webster, F., 1968: Observations of inertial-period motions in the deep sea. *Rev. Geophys.*, **6**, 473–490.

Weller, R. A., 1982: The relation of near-inertial motions observed in the mixed layer during the JASIN (1978) experiment to the local wind stress and to the quasi-geostrophic flow field. *J. Phys. Oceanogr.*, **12**, 1122–1136.